

Controlled Growth of Monodisperse Nanocrystallites in Tin(IV) Oxide Nanofilms

Samad Bazargan, Nina F. Heinig, Debabrata Pradhan, and K. T. Leung*

WATLab and Department of Chemistry, University of Waterloo, Waterloo, Ontario N2L 3G1, Canada

Received September 6, 2010; Revised Manuscript Received October 31, 2010

ABSTRACT: Uniform nanocrystalline films of tin oxide have been deposited on glass and silicon substrates by a solution spin-coating method followed by annealing under flowing oxygen at different temperatures. Complete conversion of the coated tin(IV) chloride solution to tin oxide at a post-oxygen-anneal temperature greater than 120 °C is confirmed by energy-dispersive X-ray analysis and depth-profiling X-ray photoemission measurements. Transmission electron microscopy and X-ray diffraction studies further reveal that the onset of SnO₂ nanocrystallite formation in the amorphous film occurs at 350 °C. The resulting nanocrystallites that are accompanied by the observed granular structures and voids throughout the film as a result of crystallization and grain growth exhibit a narrow size distribution. The average nanocrystallite size is found to slowly increase from 7 nm at 350 °C to 10 nm at 500 °C (likely due to a strain-limited growth mechanism) and to grow exponentially above a second onset at 500 °C with a concomitant growth of the grains and a rapid increase in the roughness of the granular films. X-ray diffraction and Raman experiments further show a largely uniform depth distribution of nanocrystallites throughout the film, with a higher density near the surface. The facile physical control in the average size of the nanocrystallites by post-oxygen-anneal temperature in a desirable size regime (7–30 nm) promises a cost-effective, easily scalable fabrication method of SnO₂ film for gas-sensing and nanoelectronic applications.

1. Introduction

Transparent conducting oxide materials have been widely used in a variety of applications due to their unique physical and chemical properties. Some of the important transparent conducting oxides are SnO₂, ZnO, In₂O₃, Ga₂O₃, and CdO.^{1,2} The wide band gap in these oxides gives rise to their transparency, while the presence of metal interstitials and oxygen deficiency in their lattices generally leads to high n-type conductivity. Transparent conducting oxides can also take up a high level of oxygen deficiency while keeping the lattice structure almost intact. Furthermore, oxygen exchange reactions on their highly chemically stable surfaces could generate strong gas sensing and catalytic activities.³ All these properties make transparent conducting oxides attractive materials for solar cells, displays, catalysts, and gas sensor applications.

The two most common phases of tin oxide (TO) are tin(II) or stannous oxide (SnO) and tin(IV) or stannic oxide (SnO₂) with tin having an oxidation state of +2 and +4, respectively. SnO₂ has a band gap of 3.6 eV and is more stable than SnO in thermal conditions of interest for most known applications of this material.^{3,4} SnO₂ has also been found to be one of the most chemically stable materials among the aforementioned transparent conducting oxide materials. Fluorine and antimony doped SnO₂ show a very low resistivity on the order of 10⁻⁴ Ω·cm, comparable to those of the highly conductive indium–tin-oxide and doped ZnO films.^{1–3} Homogeneous, pristine, or doped layers of SnO₂ with noble metal ions or their oxides are the most commonly used materials in solid-state gas sensors.⁵ SnO₂ gas sensors have a high sensitivity, and the porosity of the films and the crystallite size have proven to be very important factors in improving the sensitivity and response

time of these sensors. In particular, the gas-sensing properties of SnO₂ have been found to increase by decreasing the crystallite size below 10 nm for both pristine and doped SnO₂ sensors.^{6,7} The adsorbed gases create space-charge layers on the surface of the crystallites, which generate an electric field that bends the energy band to create a barrier for carrier transport through the film. Decreasing the size of crystallites below 10 nm makes the thickness of this space-charge layer comparable to the size of the grain, which drives the transport toward a “neck-controlled” regime or even a total carrier-depleted grain regime with further decrease in the crystallite size.^{6,8} Reducing the SnO₂ crystalline grain size and narrowing its size distribution will therefore greatly increase the sensitivity of the gas sensors.

In addition to the importance of the SnO₂ crystalline grain size for gas-sensing applications, the conductivity of the film is also of great interest to their applications as transparent conducting electrodes or active semiconducting layers in organic electronics^{9–11} and in transparent thin-film transistors.¹² There are several challenges in modifying or improving some of the properties of the SnO₂ layers for these applications. In particular, controlling the surface roughness and the uniformity of the SnO₂ film are crucial for minimizing current leakage problems in device applications, while improving the quality of the interface between the SnO₂ layer and other layers would enhance the charge transport and functionality of the device. Understanding the structural, physical, and chemical properties of SnO₂ and the changes that can be induced in its structure and consequently its other properties can offer new routes to address the challenges associated with this material.

Extensive studies have been conducted on TO films developed on different substrates by a variety of methods, including radio frequency magnetron sputtering,^{13,14} electrodeposition,¹⁵ sol–gel,^{16–19} successive ionic layer deposition,^{20,21} spray

*To whom correspondence should be addressed. E-mail: tong@uwaterloo.ca.

pyrolysis,^{22,23} and pulsed laser deposition.^{24,25} Depending on the deposition method, postannealing, calcination, or manipulation of the substrate temperature and gas pressure can be used to control the size of the crystallites and to produce the desired morphology. In the present work, we demonstrate the preparation of continuous, smooth, granular TO films on glass and Si substrates by using a simple, easily scalable spin-coating procedure followed by annealing in oxygen. We identify the onset of crystallization and the growth evolution, as well as a simple means to control the nanocrystallite size and density in the layers. Extensive characterization is also performed in order to explore the relationship of the morphology, crystallinity, and nanocrystallite size and distribution to the chemical composition and defects of the films. The present study shows that the present preparation technique could be an attractive alternative to the commonly used methods of producing nanocrystalline TO films based on spin-coating of presynthesized SnO₂ nanoparticles onto an insulating substrate.^{16,18}

2. Experimental Details

Thin uniform TO films were prepared on glass and Si substrates by spin-coating an appropriate amount of a precursor solution [first in a low-speed (600 rpm) step followed by a high-speed (1800 rpm) step for even spreading] by using a programmable spinner (Headway Research PWM32). The precursor solution consisted of 0.5–2.0 M SnCl₄·5H₂O in isopropanol. Ethanol and water have also been used as the solvent, but they do not give better results than isopropanol for glass substrates. The 2 × 2 cm² glass (Corning No. 0211) substrates (0.2 mm thick) were cleaned by thorough washing and sonication in acetone and then isopropanol. To improve the adhesion of the coating to the glass substrate, the glass was roughened by etching in a 1 M NaOH solution for 10 min followed by thorough washing and sonication in isopropanol. In the case of Si substrates, the original RCA method²⁶ was used to produce a clean Si surface with a thin oxide layer. The spin-coated films were subsequently transferred into a quartz tube furnace and annealed for 1 h in a flowing oxygen atmosphere (with a flow rate ≥ 70 sccm) at 100–900 °C, during which SnCl₄ underwent a single-replacement reaction (with O₂) to form tin oxide, SnO_x (x = 1, 2). A gentle heating ramp of 10 °C min⁻¹ was used in order to minimize the formation of cracks in the films.

The surface morphology of the films was examined by scanning electron microscopy (SEM) in a LEO FESEM 1530 microscope, while surface roughness was determined under ambient conditions by tapping-mode atomic force microscopy (AFM) in a Digital Instruments Dimension 3100 Nanoscope IV. The structure of the films was analyzed by using glancing-incidence X-ray diffraction (GIXRD) at an incidence angle of 0.3° in a PANalytical MRD X'pert Pro diffractometer using the Cu Kα line (1.54 Å) with a Cu mirror in the incident beam optics and a parallel plate collimator in the diffracted beam optics. Local nanostructures were also studied by transmission electron microscopy (TEM) in a JEOL 2010F scanning TEM operated at 200 kV. Surface composition of the as-formed films was characterized by X-ray photoelectron spectroscopy (XPS) using a Thermo-VG Scientific ESCALab 250 Microprobe with a monochromatic Al Kα source (1486.6 eV), capable of an energy resolution of 0.4–0.5 eV full width at half-maximum (fwhm). Raman vibrational spectra of the samples were measured by using a Bruker Senterra Raman spectrometer with an excitation wavelength of 532 nm and a spectral resolution of 3–5 cm⁻¹.

3. Results and Discussion

3.1. Surface Morphology and Roughness. SEM studies have been performed on all the films, of which minor charging was observed for those prepared with a postanneal temperature below 350 °C, reflecting their nonconducting nature. Subsequent EDX studies on these nonconducting films (obtained with a postannealing temperature of 120–300 °C)

revealed no detectable chlorine signal in the samples, which indicates the completion of the oxygen replacement reaction. It is important to note that the oxygen flow plays an essential role in this replacement reaction, because it drives the reaction toward completion even at a postanneal temperature as low as 120 °C. If the annealing was performed without oxygen flow, evaporation of the solvent would occur, causing recrystallization of stannic chloride salt appearing as a white powder on the glass surface. For the spin-coated film obtained with a 2 M [SnCl₄] solution and postannealing at 450 °C, continuous uniform deposition on the glass substrate was observed (Figure 1a). As is commonly found in a spin-coating process, a minor material build-up was noted near the edges of the substrate due to surface tension. The crack formation that has often been reported in sol–gel coated films^{16,19} can be minimized by optimizing the initial annealing rate. Close examination at a higher magnification of the sample postannealed at 400 °C reveals the granular morphology of the film with grain sizes below 50 nm (Figure 1b). Similar morphologies have also been obtained for films postannealed at 350, 450, and 500 °C (not shown). As shown in the cross-sectional SEM image (inset of Figure 1b, and further confirmed by low resolution TEM images in Figure 4 below), grains are also found throughout the thickness of the film, similar to that observed for the surface. For a spin speed of 1000–1800 rpm and duration of 5–10 min, the concentration of the precursor solution, [SnCl₄], used in the spin-coating process is found to play an important role in controlling the thickness of the resulting TO films (after postannealing). The film thickness can be varied from 130 nm using a 0.5 M solution to 218 nm using a 2.0 M solution, the latter of which is illustrated in the cross-sectional SEM image of the sample postannealed at 400 °C (inset of Figure 1b). Repeating the spin-coating and postannealing cycle in successive steps can be used to create thicker films, with the film thickness reproducible to within 30 nm.

Figure 1 also shows AFM images of the glass substrate with (Figure 1c) and without etching (Figure 1c, inset), and of the TO films as-deposited and upon postannealing at different temperatures on the etched glass substrates (Figure 1d–i). Table 1 summarizes the corresponding root-mean-square (rms) surface roughness of these samples over a fixed scan area of 1 μm². As expected, the surface roughness of the etched glass (Figure 1c), with a rms value of 0.4 nm, is considerably larger than that of the nonetched glass (Figure 1c, inset), with a rms value of 0.2 nm. The rms roughness of the deposited films is found to increase with increasing postanneal temperature, from 0.9 nm over 1 μm² at 250 °C to 2.2 nm over 1 μm² at 500 °C on the etched glass substrate, and to 6.6 nm over 1 μm² at 600 °C on Si substrate (Table 1). Small round grains are found to emerge on the surface of the film prepared with a postanneal at 350 °C (Figure 1f), suggesting the onset of a structural evolution at this temperature. Raising the postanneal temperature to 400, 450, and 500 °C increases the granularity of the film, with a concomitant increase in the size of these grains (Figure 1g–i) and in the rms roughness (Table 1). It should be noted that the rms roughness values of the films synthesized below 500 °C by the present method are among the smallest when compared to those of films prepared by other methods, for example, electron beam evaporation²⁷ and spray pyrolysis,^{11,22} making the present procedure not only a facile and cost-effective but also a superior method for device fabrication. Furthermore, the apparent granular structure appears homogeneous

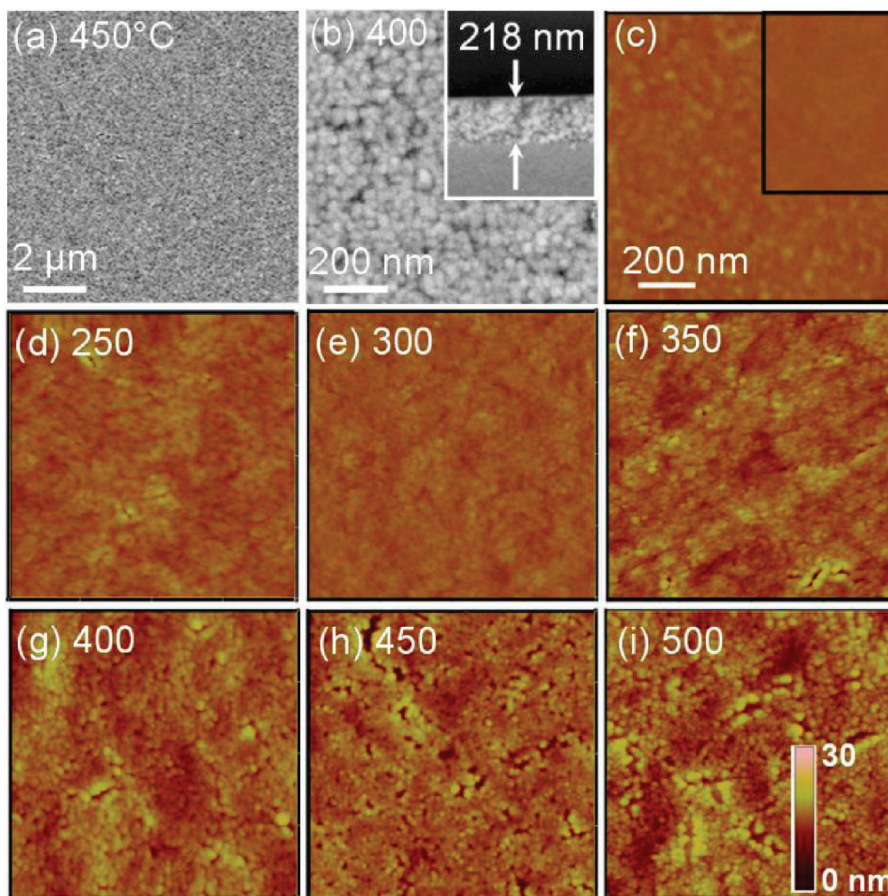


Figure 1. SEM images of tin oxide films prepared with a post-oxygen-anneal at (a) 450 °C and (b) 400 °C (with a cross-sectional image of the film shown in inset). AFM images of (c) glass substrate with and without etching (inset) and (d–i) tin oxide films prepared with post-oxygen-annealing at different temperatures. Roughness (height) scale and scale bar are the same for all the AFM images.

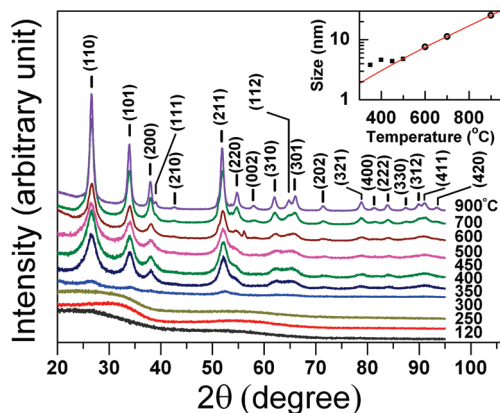


Figure 2. Glancing-incidence XRD patterns of tin oxide films prepared with different post-oxygen-anneal temperatures with peak assignments in accord with the SnO_2 reference pattern (ICDD PDF# 00-041-1445). The patterns are shown on a linear scale and have been offset for clarity. Inset shows the change in the nanocrystallite size, deduced by Scherrer analysis based on the (110) peak width, with increasing postanneal temperature. The straight line in the inset corresponds to an exponential fit to the data on the high temperature side (500–900 °C). The films obtained at 600, 700, and 900 °C are prepared on Si substrates, while the rest obtained at a lower postanneal temperature are prepared on glass substrates.

over the entire sample. This granularity along with the pores observed in the cross-sectional SEM image (inset of Figure 1b), and further shown in low-resolution TEM images

in Figure 4 below) helps to increase the surface area of the film.

3.2. Crystal Structures. Figure 2 compares the GIXRD patterns of the deposited films (spin-coated with a 2 M $[\text{SnCl}_4]$ solution) postannealed for 1 h at different temperatures. For the films obtained with a postanneal temperature below 350 °C, diffraction patterns with broad features are observed, indicating an amorphous film structure (Figure 2). On the other hand, the films obtained with a postanneal temperature at or above 350 °C exhibit prominent diffraction peaks, the peak positions and relative intensities of which are in excellent accord with the reference tetragonal SnO_2 profile (ICDD PDF# 00-041-1445). This indicates that the onset of crystallization occurs near 350 °C. The peak observed at $2\theta = 56.12^\circ$ for the sample postannealed at 600 °C and the weak shoulder at $2\theta = 51.12^\circ$ correspond to diffraction features of the Si(100) substrate. The peak intensities of the TO film obtained at 400 °C are found to be considerably higher than those at 350 °C, while a postanneal temperature in the range of 400–500 °C does not significantly increase the respective intensities. Applying the Scherrer analysis to the strongest, (110), diffraction peak of the films enables us to estimate the corresponding average crystalline grain sizes. As shown in Table 1, the average crystalline grain size is found to increase from 3.8 nm at 350 °C to 4.8 nm at 500 °C on the glass substrates. The growth trend has also been studied at higher temperatures by preparing TO films on Si substrates with postannealing at 600, 700, and 900 °C. It should be noted that deposition below 600 °C has also been performed on Si

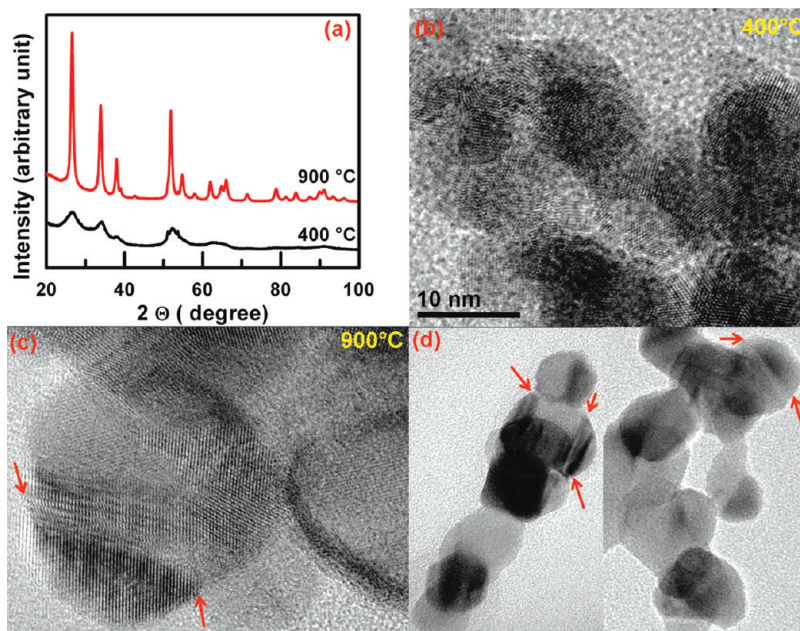


Figure 3. (a) Glancing incidence XRD profiles and (b, c, d) TEM images of a tin oxide film prepared on a Si substrate with post-oxygen anneal at 400 °C (a, b), followed by a second anneal of the same film at 900 °C (a, c, d).

Table 1. Root-Mean-Square (RMS) Surface Roughness over 1 μm^2 Area Measured by AFM, Full Width at Half Maximum (fwhm) of the (110) Peak and the Corresponding Crystallite Sizes Estimated by the Scherrer Analysis, and Compared to Those Obtained from TEM Data, for the Pristine and Etched Glass Substrate and for Tin Oxide Samples Prepared with Different Post-Oxygen-Anneal Temperatures on Etched Glass Substrates (250–500 °C) and Si Substrates (600, 700, 900 °C)

| samples | rms roughness (nm) | fwhm of the (110) peak (deg) | crystallite size from XRD (nm) | crystallite size from TEM (nm) |
|------------------------|--------------------|------------------------------|--------------------------------|--------------------------------|
| glass substrate | 0.2 ± 0.1 | NA | NA | NA |
| etched glass substrate | 0.4 ± 0.1 | NA | NA | NA |
| 250 °C | 0.9 ± 0.1 | NA | NA | NA |
| 300 °C | 0.7 ± 0.1 | NA | NA | NA |
| 350 °C | 1.6 ± 0.3 | 2.55 | 3.8 | 6.6 ± 1.0 |
| 400 °C | 1.7 ± 0.3 | 2.14 | 4.6 | 8.7 ± 1.6 |
| 450 °C | 2.2 ± 0.3 | 2.24 | 4.4 | 9.4 ± 1.4 |
| 500 °C | 2.2 ± 0.3 | 2.08 | 4.8 | 9.7 ± 1.5 |
| 600 °C | 6.6 ± 2.0 | 1.47 | 7.6 | NA |
| 700 °C | NA | 1.12 | 11.3 | NA |
| 900 °C | NA | 0.72 | 25.5 | 30 ± 9.9 |

substrate, and the resulting films are found to exhibit morphology and properties similar to those prepared on glass substrates. This similarity is likely due to the existing native oxide layer (~ 10 nm thick) on the Si substrates (as a result of the RCA cleaning method). The corresponding XRD patterns (Figure 2) show an increase in the peak intensities along with a notable decrease in the peak width. Scherrer analysis further indicates a considerable increase in the average nanocrystallite size to 7.6, 11.3, and 25.5 nm with the respective increasing postanneal temperature (Table 1).

The observed trends in the intensities of the diffraction peaks and the average nanocrystallite sizes with increasing postanneal temperature suggest a two-step growth mechanism with onsets at 350 and 500 °C. Depending on the synthesis methods, there are different reports about the onset temperature of crystallization for SnO_2 . In particular, Shukla et al.¹⁹ annealed a dip-coated film at 600 °C to create nanocrystallites in the layer (as shown in their TEM images), while

Jin et al.¹⁷ obtained crystalline samples upon annealing a spin-coated tin oxide gel at 400 °C. Chang et al.¹⁵ reported the formation of a crystalline phase in electrodeposited films, which they subsequently annealed at 400 °C for 4 h in order to increase the crystallinity of the samples. The presently observed crystallization onset at 350 °C is therefore in good accord with these earlier studies. Above the onset of nanocrystallite formation at 350 °C, a minor increase in the post-anneal temperature, for example, 400 °C, dramatically increases the amount of crystalline material. Further increase of the postanneal temperature to 450 and 500 °C, however, does not significantly change the amount of crystalline material. In order to determine whether the conversion of amorphous to crystalline TO is complete, we compare the XRD patterns of a TO film prepared on a Si substrate, in a separate experiment, with postannealing at 400 °C before and after a second postanneal at 900 °C (Figure 3a). The apparent increase in the peak area of the (110) diffraction peak after the second anneal at a higher temperature (900 °C) indicates that a substantial amount of amorphous phase remains in the TO films obtained with a postanneal at 400–500 °C (Figure 3a). However, further annealing a sample obtained by postannealing at 400 °C (for 1 h) for extended time periods (24 and 96 h) at the same postanneal temperature (400 °C) produces essentially unchanged XRD patterns, that is, without any discernible changes in the peak intensity and width (Supporting Information, Figure S1). These experiments show that although the amorphous-to-crystalline conversion in this temperature range (400–500 °C) is incomplete, no further detectable nucleation and nanocrystallite growth occur with prolonged annealing at the same temperature. This indicates the heterogeneous nature of nucleation within the amorphous TO phase and that the resulting nanocrystallites in the amorphous matrix are restrained from further growth. The nanocrystallite size also exhibits a very slow increase with increasing postanneal temperature from 3.8 nm at 350 °C to 4.4–4.8 nm at 400–500 °C (inset of Figure 2). However, increasing the postanneal

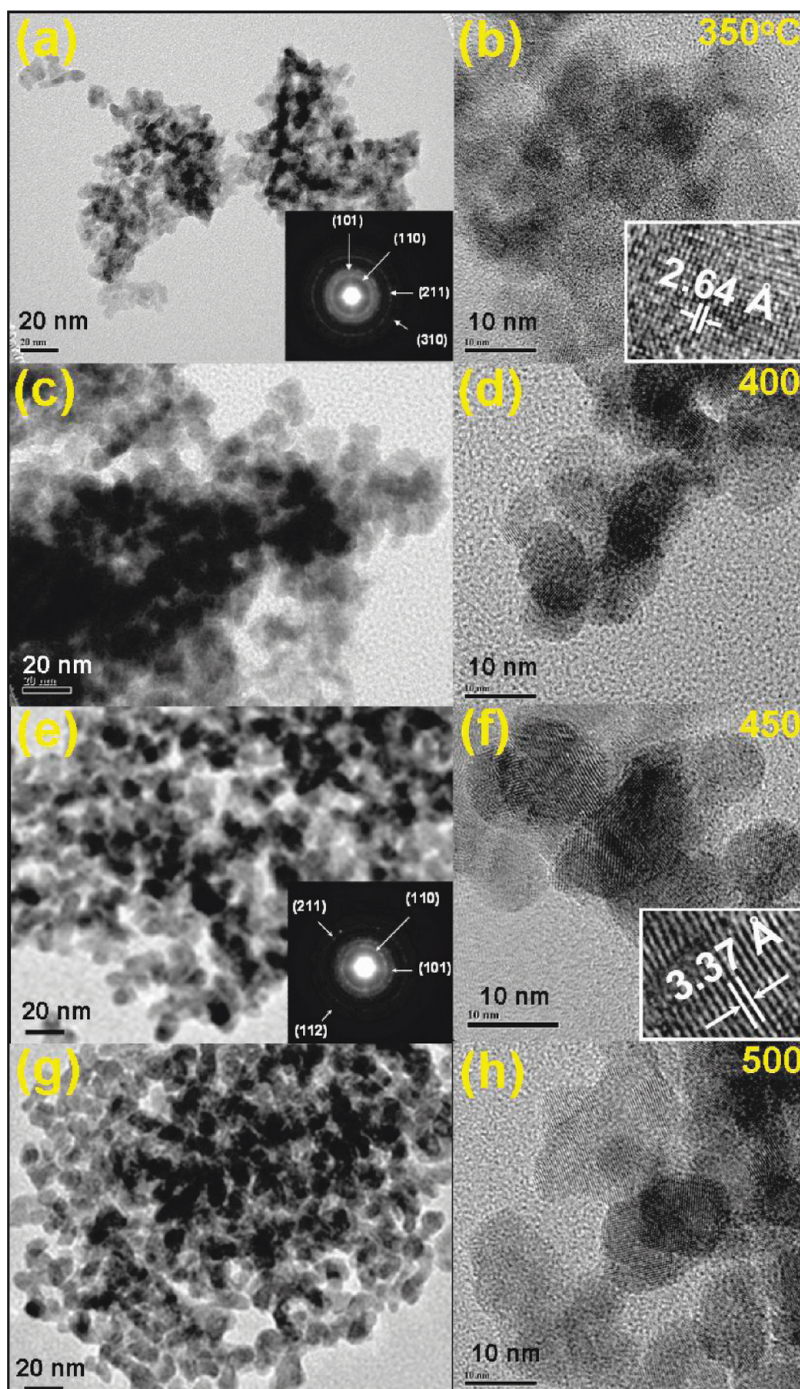


Figure 4. TEM images of the tin oxide films prepared on glass substrates with post-oxygen-annealing at (a, b) 350 °C, (c, d) 400 °C, (e, f) 450 °C and (g, h) 500 °C. Insets show the respective magnified areas of the images, with the lattice planes and their spacings (b, f), and selected area electron diffraction patterns, with the crystalline planes identified for individual rings (a, e) for samples prepared with postannealing at 350 and 450 °C.

temperature to 600, 700, and 900 °C leads to an exponential increase in the nanocrystallite size, along with a concomitant decrease in the amount of amorphous phase, indicating a new growth mechanism above 500 °C. We hypothesize that the change in density near the nucleation sites during the conversion of amorphous phase to crystalline phase creates strain, which in turn limits the nanocrystallite growth to less than 5 nm in size below the second onset temperature (500 °C). Above 500 °C, sufficient energy is available to overcome the barrier in this “strain-limited” growth step, and the subsequent growth step follows the Arrhenius-like (exponential) trend.

Figure 4 shows the bright-field TEM images of the TO films obtained on the glass substrates with different post-anneal temperatures. The TEM images have been obtained from different parts of the film to ensure a general sampling of the entire film. Evidently, the size distributions of the nanocrystallites obtained over the postanneal temperature range (350–500 °C) for the present TEM study appear to be quite narrow (typically ± 1.5 nm). The as-grown grains are generally found to be spherical, with a diameter smaller than 10 nm. This granular structure also leads to formation of pores throughout the film thickness. This is consistent with

the observed spherical grain morphology and the increasing trend in the surface roughness of the films with increasing postanneal temperature, as observed in the respective SEM and AFM images (Figure 1). The average sizes of these crystalline grains are estimated from the high-resolution TEM images (Figure 4, right) by fitting circles or ellipses around the crystallites, and they are summarized in Table 1. The average grain size is found to increase from 6.6 nm at 350 °C to 8.7–9.7 nm in the 400–500 °C range. The present TEM analysis gives a similar trend of increasing crystallite size with increasing postanneal temperature, but with larger nanocrystallite sizes than those given by the XRD Scherrer analysis. Given that peak broadening in XRD is due to both crystallite size and local defects and strain in the nanocrystallites, Scherrer analysis will give smaller grain sizes for nanocrystalline films with more crystalline defects. The discernibly larger grain sizes extracted from the TEM images than those obtained from the XRD patterns therefore suggest the presence of a considerable amount of defects in the nanocrystallites.

The lattice spacings are also measured from the high-resolution TEM images shown for the samples obtained with postanneal temperatures of 350 and 450 °C (insets of Figure 4b,f). The corresponding lattice spacings of 2.64 and 3.37 Å are well matched to the respective lattice spacings of the (101) plane (2.6427 Å) and (110) plane (3.347 Å) of the reference bulk tetragonal SnO₂ (ICDD PDF# 00-041-1445). These two lattice spacings are the largest found in the SnO₂ structure, making them the easiest to identify in the TEM images. Careful inspection of the lattice spacings indicates that within a single grain, the lattice spacings may vary around an average value, indicating the presence of crystalline defects, such as vacancies, dislocations, and local strains. The high-resolution images therefore support our conclusion that the observed larger average crystalline grain size than those deduced by Scherrer XRD analysis is largely due to the presence of crystalline defects. Closer examination of the high-resolution images reveals the presence of a large density of point and line defects in the observed crystallites, which is particularly evident in the sample postannealed at 350 °C (Figure 4b). The observed crystallites for the samples prepared at temperatures below 500 °C have less distinct boundaries, and in spite of the large number of defects appear to exhibit a single crystalline orientation individually (Figures 3 and 4). However, for the sample postannealed at 900 °C, there are individual crystallites with different crystalline orientations (Figure 3c,d). Evidently, the regions with different orientations are separated by contrasting fringes (marked by arrows), which show the change in the crystal orientation and the stress and defect lines in their boundary. Moreover, the distorted shape of the crystallite, together with the observed different crystal orientations at which distortions are observed, clearly show that fusion of crystallites with different initial crystalline orientations could be a plausible mechanism for grain growth at a higher temperature.

For the samples obtained with postanneal temperatures of 350 °C (Figure 4a) and 450 °C (Figure 4e), distinct diffraction rings originating from different planes found in the respective selected area electron diffraction patterns further indicate the polycrystalline nature of the SnO₂ phase in the sample. The bright rings at the center of the respective patterns correspond to the (110) and (101) planes, while the (211) ring is also visible in both patterns. Similar diffraction patterns exhibiting the (110), (101), and (211) planes have also been reported by

Chang et al.¹⁵ and Chen et al.²⁸ Additional weak (310) and (112) rings are also observed for the samples postannealed at 350 and 450 °C, respectively. The observed diffraction rings indicate the presence of only polycrystalline phase of SnO₂, without a discernible amount of crystalline SnO or metallic Sn, in good accord with the GIXRD results.

3.3. Composition. Our X-ray diffraction data indicate that there are significant amounts of both crystalline and amorphous phases present in the TO film obtained with postannealing at 400 °C (on a glass substrate). Unlike the films obtained at a higher postanneal temperature of 600–900 °C (on a Si substrate), this granular film contains monodisperse nanocrystallites with sizes below 10 nm, which are of potential interest to new applications and are especially desirable for gas-sensing applications. This film also represents the type of stable TO films with similar structural and composition characteristics that can be obtained on a transparent, low-heat resistant substrate like glass in this temperature range (400–500 °C). We therefore conduct further composition analysis of this film by depth-profiling XPS. The survey spectrum of the film (Supporting Information, Figure S2) shows prominent Sn and O features, with no discernible intensity for Cl features, confirming the completion of the replacement reaction.

Figure 5a shows the XPS spectra of the Sn 3d_{5/2} and O 1s regions at different sputtering times for the TO film obtained with postannealing at 400 °C (Figure 1b,g). The Sn 3d_{5/2} peak at 487.4 eV for the as-prepared film starts to shift to a lower binding energy after 60 s of sputtering and settles at 487.0 eV for longer sputtering times (> 120 s). This minor shift toward a lower binding energy is also observed for the O 1s peak, from 531.3 eV for the as-prepared film to 530.8 eV upon sputtering for > 120 s. These binding energy shifts in the Sn 3d_{5/2} and O 1s peaks may be due to surface charging caused by the presence of a carbonaceous layer as a result of sample handling in air. A closer examination of the spectra (Figure 5a) reveals the presence of a high-energy tail of the O 1s peak, which has been attributed to “chemisorbed oxygen” on the surface by Szuber et al.²⁹ in their XPS study of the surface treatment of SnO₂. To assign the Sn 3d_{5/2} features, we have measured the XPS spectra of SnO₂ and SnO powders (Aldrich, 99.9% and 99% purity, respectively) as reference, which, after sputtering for 200 s to remove the carbonaceous layers, exhibit Sn 3d_{5/2} binding energies of 487.0 and 486.6 eV, respectively. In accord with these reference spectra (Supporting Information, Figure S3), we assign the observed Sn 3d_{5/2} peak at 487.0 eV to Sn⁴⁺ (in SnO₂). This assignment is also consistent with the reported binding energy values for tin oxide synthesized by different procedures,^{30–32} all found with an energy difference of less than 1 eV between the Sn⁴⁺ and Sn²⁺ states.

In Figure 5, we also plot, as a function of sputtering time, the relative peak intensities of Sn 3d_{5/2} (at 487.0 eV) and O 1s (at 530.8 eV), as well as the corresponding O-to-Sn ratio obtained after appropriate correction by the respective sensitivity factors (4.725 for Sn 3d_{5/2} and 0.711 for O 1s).³³ The presence of chemisorbed oxygen could account for the slightly higher stoichiometric ratio (2.1) found for the as-prepared sample. After sputtering for 60 s, a considerable reduction in the O 1s peak intensity is observed primarily due to the removal of the high binding energy tail, which also supports the presence of chemisorbed oxygen on the surface of the as-prepared film. On the other hand, sputtering for 60 s has markedly increased the Sn 3d_{5/2} peak intensity by 20%, which then slowly decreases with increasing sputtering

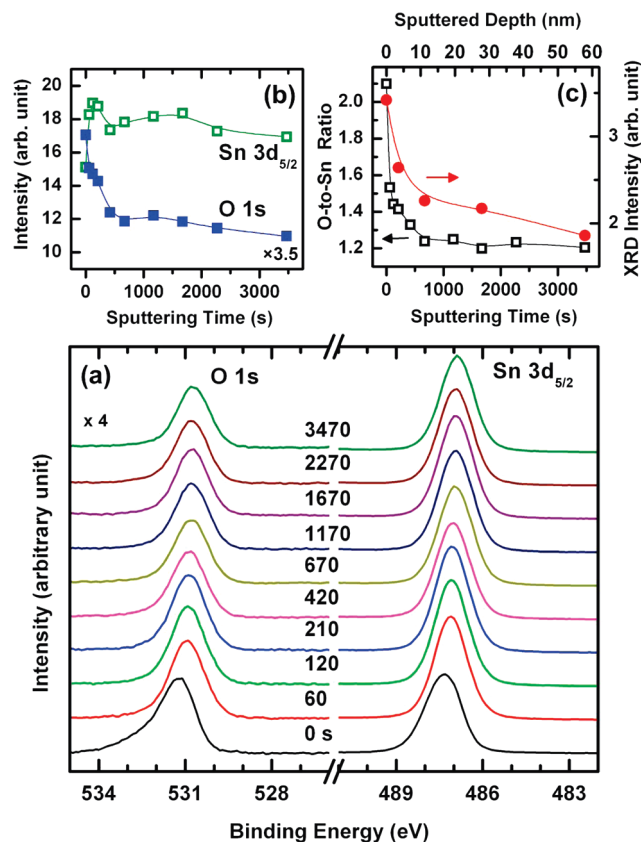


Figure 5. (a) XPS spectra of the O 1s and Sn 3d_{5/2} regions for the as-deposited tin oxide film prepared with post-oxygen-annealing at 400 °C as a function of sputtering time, (b) relative intensities for O 1s and Sn 3d_{5/2} peaks, and (c) comparison of the corresponding O-to-Sn ratio (after appropriate correction of the relative sensitivity factors) to the relative area intensity of the (110) XRD peak as a function of sputtering time (with the corresponding sputtering depth shown at top).

(Figure 5b). These intensity changes reduce the stoichiometric ratio to ~ 1.6 (Figure 5c). Further sputtering to 120 and 210 s causes minor changes to the O 1s and Sn 3d_{5/2} intensities and reduces the ratio further to 1.4. The observed O-to-Sn ratio of 1.4–1.6 is in accord with those reported for TO films prepared by different methods.^{29,34,35} Continued sputtering to greater than 400 s reduces the ratio to 1.3–1.2, which remains essentially unchanged even upon sputtering to 3470 s. It should be noted that our reference SnO₂ powder sample had a similar O-to-Sn ratio after long sputtering (1.3 after 400 s). Furthermore, like the reference SnO₂ powder sample, the positions of the Sn 3d_{5/2} and O 1s peaks for our TO sample remain effectively unchanged with continued sputtering.

The smaller than expected stoichiometric ratio has been discussed in the literature and is attributed to preferential sputtering of O compared to Sn atoms in SnO₂ films.^{34–36} In addition, it has been reported that sputtering of SnO powder causes reduction of Sn²⁺ (at 485.6 eV binding energy) to metallic Sn⁰ with a lower binding energy (483.8 eV),³⁰ which has also been observed in the spectrum of our reference SnO powder with a shift to the binding energy of 485.0 eV. Evidently, SnO₂ is very stable and reduction to lower oxidation states at our sputtering energy of 3 kV was not observed. The absence of a metallic Sn⁰ peak in the TO film even after sputtering for 3470 s therefore further supports the conclusion that SnO₂ is the predominant composition throughout the film.

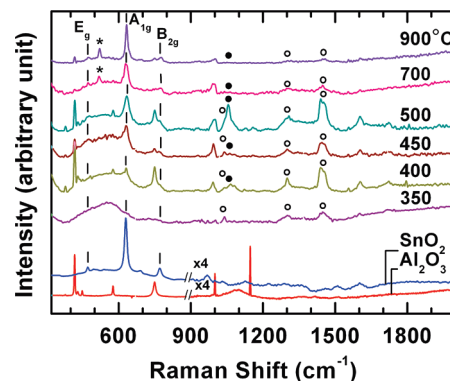


Figure 6. Comparison of Raman spectra of the tin oxide films prepared with post-oxygen-annealing at 350, 400, 450, 500, 700, and 900 °C with reference spectra of SnO₂ powders and sapphire support (scales for the 900–2000 cm⁻¹ region for the reference sapphire support and SnO₂ powders have been changed for clarity). Open and solid circles mark the observed additional sample peaks not found in the reference spectra, while the star symbol identifies the peak position of crystalline Si. Spectra are offset for clarity.

In order to determine the distribution of nanocrystallites as a function of depth, we collected GIXRD profiles at selected sputtering times, all of which resemble the profile for the sample obtained with postannealing at 400 °C (shown in Figure 2). Figure 5c compares the relative intensity of the (110) XRD peak with the respective O-to-Sn ratio (determined from our XPS experiment) as a function of sputtering depth. In a separate experiment, we estimated the sputtering rate to be ~ 1 nm/min by completely sputtering away a test TO thin film postannealed at 400 °C on a glass substrate. Evidently, the crystalline phase persists after removal of $\sim 20\%$ of the film, which suggests that the formation of nanocrystallites occurs throughout the thickness of the layer. However, the intensity reduction of the (110) diffraction peak is found to be more pronounced for the first 670 s of sputtering (Figure 5c), suggesting the presence of a higher density of nanocrystallites in the near-surface region compared to the bulk of the film (or ion-sputtering induced damage to the nanocrystallites at the near-surface).

In order to further elucidate the role of defects and the amorphous phase in the SnO₂ nanocrystalline film formation, we perform Raman spectroscopy on the samples prepared with postannealing at 350, 400, 450, and 500 °C on glass substrates and at 700 and 900 °C on Si substrates. The TO films were scraped off from the glass/Si substrates and transferred to a sapphire support in order to avoid the large background scattering from the substrate and to provide more reflection from the collected film material than the as-deposited transparent TO film. Figure 6 compares the Raman spectra of the TO films with the reference spectra of SnO₂ powders and of the sapphire support. Evidently, an intense broad band in the 400–800 cm⁻¹ region is observed in the spectra for the TO films obtained with the postanneal temperature between 350 and 700 °C. For the TO film prepared with postannealing at 350 °C, the observed broad band appears to center near 560 cm⁻¹, and there is no discernible peak associated with crystalline SnO₂ observed in this range (positions of these SnO₂ characteristic peaks are marked by bars in Figure 6). For the TO films prepared with postannealing at 400–900 °C, new peaks are found to emerge on top of the observed broad band. Evidently, the well-resolved peak at 634 cm⁻¹ is in good accord with the intense

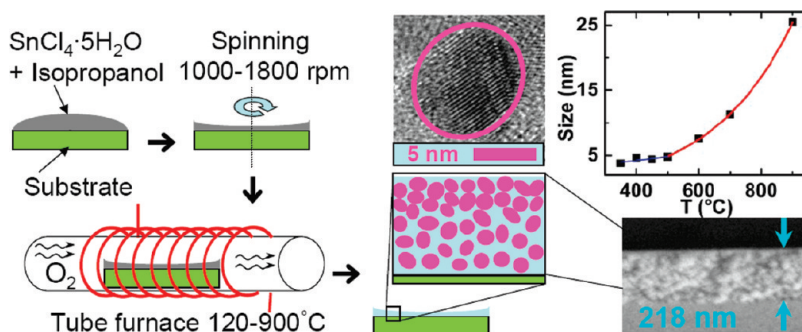


Figure 7. Schematic summary of the spin-cast-postannealing method for synthesizing tin oxide film, and the resulting distribution and size-temperature relation of nanocrystallites in the amorphous matrix.

characteristic A_{1g} peak at 631 cm^{-1} of SnO_2 powder. The relative intensity of this peak is found to increase with the postanneal temperature. In spite of the considerably lower intensities, the other two characteristic SnO_2 peaks at 473 and 772 cm^{-1} , corresponding respectively to E_g and B_{2g} modes, are also observed, with the latter near a prominent sapphire feature at 750 cm^{-1} . Our characteristic SnO_2 Raman peaks and the observed broad band are in good agreement with the results for the SnO_2 nanoparticles calcinated at different temperatures reported by Dieguez et al.³⁷ The Raman spectrum of the sample prepared at $350 \text{ }^\circ\text{C}$ does not show any of the characteristic peaks of the crystalline SnO_2 phase. This is consistent with our XRD result (Figure 2), which shows that the TO film prepared at the crystallization onset ($350 \text{ }^\circ\text{C}$) contains a very small amount of crystalline material with small nanocrystallite size of 3.8 nm . The observed broad band at $400\text{--}800 \text{ cm}^{-1}$ and the features at 1040 , 1300 , and 1440 cm^{-1} (open circles, Figure 6) are therefore signatures of defects and the amorphous phase, which constitutes a significant proportion of the TO films prepared at $350\text{--}500 \text{ }^\circ\text{C}$. For the films postannealed at $400\text{--}500 \text{ }^\circ\text{C}$, an additional Raman feature is observed at 1055 cm^{-1} (solid circles, Figure 6), and this new feature could be attributed to a nanocrystalline surface mode or to an interaction between the nanocrystalline and amorphous regions. These amorphous-phase-related features are not observed in the reference spectrum of SnO_2 powders. For TO films prepared at 700 and $900 \text{ }^\circ\text{C}$, the intensities of these amorphous-phase-related features have evidently diminished substantially, which is consistent with the onset of the exponential nanocrystallite growth step above $500 \text{ }^\circ\text{C}$ and the corresponding decrease in proportion to the amount of the amorphous phase in the TO films. Dieguez et al. have attributed the broad Raman band that they observed in the $400\text{--}800 \text{ cm}^{-1}$ for SnO_2 nanoparticles to overlapping disorder-activated surface modes.³⁷ While the nature of the other Raman features observed at 1040 , 1055 , 1300 , and 1440 cm^{-1} remains unknown, it appears likely that they are due to inter-grain or interfacial defect/disorder activated modes resulting from the nanocrystallite growth in an amorphous matrix or from the amorphous phase itself. More detailed investigations would be of interest to further elucidate these spectroscopic phenomena.

4. Summary

A simple facile method, involving spin-coating a SnCl_4 solution followed by post-oxygen-annealing at $350\text{--}500 \text{ }^\circ\text{C}$, has been developed for synthesizing uniform granular TO films with monodisperse nanocrystallites of $7\text{--}10 \text{ nm}$ in size (dia.) on glass substrates (Figure 7). The present method is

easily scalable for any large-area thin-film deposition and can be used for other substrates including silicon. The resulting films are found to be granular throughout the thickness of the films, with the rms surface roughness ($1.6\text{--}2.2 \text{ nm}$) among the smallest of the reported TO films. The XRD data shows the formation of SnO_2 nanocrystallites in an amorphous matrix with increasing postanneal temperature above the onset at $350 \text{ }^\circ\text{C}$. Furthermore, the nanocrystallite size is found to increase slowly from 7 nm at $350 \text{ }^\circ\text{C}$ to 10 nm at $500 \text{ }^\circ\text{C}$, likely due to a strain-limited growth mechanism, and exponentially above a second onset at $500 \text{ }^\circ\text{C}$. The corresponding TEM measurements give a similar trend in the nanocrystallite size with increasing postanneal temperature, while the generally larger sizes determined from TEM than those by XRD Scherrer analysis indicate the presence of defects in the nanocrystallites. The TEM result also confirms the remarkably narrow size distribution of nanocrystallites obtained in the strain-limited growth regime ($350\text{--}500 \text{ }^\circ\text{C}$). Depth-profiling XPS study supports the single-replacement reaction as the synthesis mechanism, and the complete conversion of the precursor SnCl_4 to SnO_2 throughout the entire film. The companion XRD data obtained at different sputtering depths shows a relatively uniform density with increasing depth (i.e., throughout the film) except near the surface where a higher density of nanocrystallites is found. The intensity increase in the characteristic Raman features for SnO_2 below 900 cm^{-1} with increasing postanneal temperature is consistent with the observed nanocrystallite growth. The presence of defects and the disordered amorphous phase could give rise to the broad band at $400\text{--}800 \text{ cm}^{-1}$ and the other Raman peaks observed above 1000 cm^{-1} , which begin to diminish with increasing postanneal temperature at $500 \text{ }^\circ\text{C}$. Simple control of nanocrystallite growth with postanneal temperature in the $7\text{--}10 \text{ nm}$ average size range with a narrow size distribution and a relatively uniform bulk density makes the present method of synthesizing SnO_2 nanocrystalline film particularly useful for gas-sensing applications. Further increase in the nanocrystallite size to 25 nm and greater crystallinity in the film can also be of potential interest to solar cell and nanoelectronic applications.

Supporting Information Available: Figure S1: Glancing-incidence XRD patterns of a tin oxide film after long anneals; Figure S2: XPS survey spectra of tin oxide films; Figure S3: Sn $3d_{5/2}$ and O $1s$ reference spectra of SnO_2 and SnO powders. This material is available free of charge via the Internet at <http://pubs.acs.org>.

References

- (1) Gordon, R. G. Criteria for choosing transparent conductors. *MRS Bull.* **2000**, *25*, 52.
- (2) Minami, T. Transparent conducting oxide semiconductors for transparent electrodes. *Semicond. Sci. Technol.* **2005**, *20*, S35.

- (3) Batzill, M.; Diebold, U. The surface and materials science of tin oxide. *Prog. Surf. Sci.* **2005**, *79*, 47.
- (4) Agekyan, V. T. Spectroscopic properties of semiconductor crystals with direct forbidden energy gap. *Phys. Status Solidi A* **1977**, *43*, 11.
- (5) Yamazoe, N.; Kurokawa, Y.; Seiyama, T. Effects of additives on semiconductor gas sensors. *Sensor. Actuat.* **1983**, *4*, 283.
- (6) Seal, S.; Shukla, S. Nanocrystalline SnO₂ gas sensors in view of surface reactions and modifications. *JOM-J Min. Met. M. S.* **2002**, *54*, 35.
- (7) Yamazoe, N. New approaches for improving semiconductor gas sensors. *Sensor. Actuat. B* **1991**, *5*, 7.
- (8) Barsan, N.; Weimar, U. Conduction model of metal oxide gas sensors. *J. Electroceram.* **2001**, *7*, 143.
- (9) Marks, T. J.; Veinot, J. G. C.; Cui, J.; Yan, H.; Wang, A.; Edleman, N. L.; Ni, J.; Huang, Q.; Lee, P.; Armstrong, N. R. Progress in high work function TCO OLED anode alternatives and OLED nanopixelation. *Synth. Met.* **2002**, *127*, 29.
- (10) Guzman, G.; Dahmani, B.; Puetz, J.; Aegerter, M. A. Transparent conducting sol-gel ATO coatings for display applications by an improved dip coating technique. *Thin Solid Films* **2006**, *502*, 281.
- (11) Bolink, H. J.; Coronado, E.; Repetto, D.; Sessolo, M. Air stable hybrid organic-inorganic light emitting diodes using ZnO as the cathode. *Appl. Phys. Lett.* **2007**, *91*, 223501.
- (12) Wang, L.; Yoon, M. H.; Lu, G.; Yang, Y.; Facchetti, A.; Marks, T. J. High-performance transparent inorganic-organic hybrid thin-film n-type transistors. *Nat. Mater.* **2006**, *5*, 893.
- (13) Chowdhuri, A.; Gupta, V.; Sreenivas, K.; Kumar, R.; Mozumdar, S.; Patanjali, P. K. Response speed of SnO₂-based H₂S gas sensors with CuO nanoparticles. *Appl. Phys. Lett.* **2004**, *84*, 1180.
- (14) Kim, T. W.; Lee, D. U.; Yoon, Y. S. Microstructural, electrical, and optical properties of SnO₂ nanocrystalline thin films grown on InP(100) substrates for applications as gas sensor devices. *J. Appl. Phys.* **2000**, *88*, 3759.
- (15) Chang, S. T.; Leu, I. C.; Hon, M. H. Preparation and characterization of nanostructured tin oxide films by electrochemical deposition. *Electrochem. Solid State* **2002**, *5*, C71.
- (16) Wu, N. L.; Wang, S. Y.; Rusakova, I. A. Inhibition of crystallite growth in the sol-gel synthesis of nanocrystalline metal oxides. *Science* **1999**, *285*, 1375.
- (17) Jin, Z.; Zhou, H.; Jin, Z.; Savinell, R. F.; Liu, C. Application of nano-crystalline porous tin oxide thin film for CO sensing. *Sensor. Actuat. B* **1998**, *52*, 188.
- (18) Sakai, G.; Baik, N. S.; Miura, N.; Yamazoe, N. Gas sensing properties of tin oxide films fabricated from hydrothermally treated nanoparticles: Dependence of CO and H₂ response on film thickness. *Sensor. Actuat. B* **2001**, *77*, 116.
- (19) Shukla, S.; Patil, S.; Kuiry, S. C.; Rahman, Z.; Du, T.; Ludwig, L.; Parish, C.; Seal, S. Synthesis and characterization of sol-gel derived nanocrystalline tin oxide thin film as hydrogen sensor. *Sensor. Actuat. B* **2003**, *96*, 343.
- (20) Korotcenkov, G.; Macsanov, V.; Brinzari, V.; Tolstoy, V.; Schwank, J.; Cornet, A.; Morante, J. Influence of Cu-, Fe-, Co-, and Mn-oxide nanoclusters on sensing behavior of SnO₂ films. *Thin Solid Films* **2004**, *467*, 209.
- (21) Korotcenkov, G.; Tolstoy, V.; Schwank, J. Successive ionic layer deposition (SILD) as a new sensor technology: synthesis and modification of metal oxides. *Meas. Sci. Technol.* **2006**, *17*, 1861.
- (22) Subramanian, N. S.; Santhi, B.; Sundareswaran, S.; Venkatakrisnan, K. S. Studies on spray deposited SnO₂, Pd:SnO₂ and F:SnO₂ thin films for gas sensor applications. *Synth. React. Inorg., Met.-Org., Nano-Met. Chem.* **2006**, *36*, 131.
- (23) Brinzari, V.; Korotcenkov, G.; Golovanov, V. Factors influencing the gas sensing characteristics of tin dioxide films deposited by spray pyrolysis: Understanding and possibilities of control. *Thin Solid Films* **2001**, *391*, 167.
- (24) El Khakani, M. A.; Dolbec, R.; Serventi, A. M.; Horrillo, M. C.; Trudeau, M.; Saint-Jacques, R. G.; Rickerby, D. G.; Sayago, I. Pulsed laser deposition of nanostructured tin oxide films for gas sensing applications. *Sensor. Actuat. B* **2001**, *77*, 383.
- (25) Chen, Z. W.; Wu, C. M. L.; Shek, C. H.; Lai, J. K. L.; Jiao, Z.; Wu, M. H. Pulsed laser ablation for tin dioxide: Nucleation, growth, and microstructures. *Crit. Rev. Solid State* **2008**, *33*, 197.
- (26) Kern, W. *Handbook of Semiconductor Wafer Cleaning Technology Science, Technology, and Applications*; William Andrew Publishing/Noyes: Norwich, NY, 1993.
- (27) Pan, X. Q.; Fu, L. Tin oxide thin films grown on the (-1012) sapphire substrate. *J. Electroceram.* **2001**, *7*, 35.
- (28) Chen, Z. W.; Lai, J. K. L.; Shek, C. H.; Chen, H. D. Production of amorphous tin oxide thin films and microstructural transformation induced by heat treatment. *Appl. Phys. A: Mater. Sci. Process.* **2005**, *81*, 1073.
- (29) Szuber, J.; Czempik, G.; Larciprete, R.; Koziej, D.; Adamowicz, B. XPS study of the L-CVD deposited SnO₂ thin films exposed to oxygen and hydrogen. *Thin Solid Films* **2001**, *391*, 198.
- (30) Themlin, J. M.; Chtaib, M.; Henrard, L.; Lambin, P.; Darville, J.; Gilles, J. Characterization of tin oxides by x-ray-photoemission spectroscopy. *Phys. Rev. B* **1992**, *46*, 2460.
- (31) Batzill, M.; Kim, J.; Beck, D. E.; Koel, B. E. Epitaxial growth of tin oxide on Pt(111): Structure and properties of wetting layers and SnO₂ crystallites. *Phys. Rev. B* **2004**, *69*, 165403.
- (32) Jimenez, V. M.; Mejias, J. A.; Espinos, J. P.; Gonzalez-Elipe, A. R. Interface effects for metal oxide thin films deposited on another metal oxide II. SnO₂ deposited on SiO₂. *Surf. Sci.* **1996**, *366*, 545.
- (33) Moulder, J. F.; Stickle, W. F.; Sobol, P. E.; Bomben, K. D. *Handbook of X-ray Photoelectron Spectroscopy*; Chastain, J., Ed.; Perkin-Elmer Corporation: Eden Prairie, MN, USA, 1992.
- (34) Cox, D. F.; Fryberger, T. B.; Semancik, S. Oxygen vacancies and defect electronic state on the SnO₂(110)-1 × 1 surface. *Phys. Rev. B* **1988**, *38*, 2072.
- (35) Themlin, J. M.; Gilles, J. M.; Johnson, R. L. Oxygen 2s spectroscopy of tin oxides with synchrotron radiation-induced photoemission. *J. Phys. IV France* **1994**, *04*, C9-183.
- (36) Kwoka, M.; Ottaviano, L.; Passacantando, M.; Santucci, S.; Szuber, J. XPS depth profiling studies of L-CVD SnO₂ thin films. *Appl. Surf. Sci.* **2006**, *252*, 7730.
- (37) Dieguez, A.; Romano-Rodriguez, A.; Vila, A.; Morante, J. R. The complete Raman spectrum of nanometric SnO₂ particles. *J. Appl. Phys.* **2001**, *90*, 1550.